Volume 12
Number 3
21 January 2024
Pages 1325–1864

Journal of Materials Chemistry A

Materials for energy and sustainability

rsc.li/materials-a

ISSN 2050-7488

ROYAL SOCIETY
OF **CHEMISTRY**

PAPER
Wee-Jun Ong *et al.*
All-in-one ultrathin nanoporous $ZnIn_2S_4$ with ameliorated photoredox capability: harvesting electron–hole pairs in cooperative hydrogen and benzaldehyde production

Journal of
Materials Chemistry A

ROYAL SOCIETY
OF CHEMISTRY

PAPER

View Article Online
View Journal | View Issue

Check for updates

Cite this: *J. Mater. Chem. A*, 2024, **12**, 1453

All-in-one ultrathin nanoporous $ZnIn_2S_4$ with ameliorated photoredox capability: harvesting electron–hole pairs in cooperative hydrogen and benzaldehyde production†

Grayson Zhi Sheng Ling,[ab] Steven Hao Wan Kok,[c] Peipei Zhang,[d] Tan Ji Siang,[ab] Choon Yian Haw,[abd] Lling-Lling Tan,[c] Binghui Chen[abde] and Wee-Jun Ong*[abdef]

The coupling of photoredox reactions utilizing both photogenerated electrons and holes has garnered significant attention for producing high-energy-density fuels and value-added products at the same time. In this work, all-in-one porous ultrathin $ZnIn_2S_4$ nanosheets were developed *via* a facile one-pot solvothermal method by carefully tuning the concentration of trisodium citrate in the synthesis medium. With the appropriate amount of trisodium citrate, the morphology structure of $ZnIn_2S_4$ can be modulated into 4–6 nm ultrathin layered sheets with noticeable nanopores of 10–70 nm, which exposes more active sites for the redox activity. The resultant cocatalyst-free $ZnIn_2S_4$ system was successfully employed in the photocatalytic H_2 evolution coupled with benzyl alcohol oxidation to produce H_2 fuel and benzaldehyde in the absence of sacrificial agents. The porous $ZnIn_2S_4$ nanosheets with ameliorated light absorption and enhanced redox capability achieved an optimal hydrogen yield of 22.2 mmol g^{-1} under 4 h simulated sunlight irradiation (AM 1.5), double that of its pristine form, resulting in an apparent quantum efficiency (AQE) value of 5.41% at 380 nm and a solar-to-hydrogen (STH) value of 0.204%. Interestingly, a highly selective (96%) benzaldehyde production of 0.33 mmol h^{-1} was observed concurrently with simultaneous benzyl alcohol conversion. *In situ* electron paramagnetic resonance (EPR) reveals that the high-selectivity benzaldehyde formation is attributed to the carbon-centered (Cα) radical-induced pathway with the direct involvement of the photogenerated holes in the C–H bond activation. Overall, this study highlights the importance of the morphology–activity relationship, providing valuable insights for the development of superior all-in-one ultrathin photocatalysts toward ameliorated dual-redox photocatalytic reactions.

Received 16th July 2023
Accepted 11th September 2023

DOI: 10.1039/d3ta04204a

rsc.li/materials-a

1. Introduction

The utilization of solar energy through photocatalytic conversion shows potential as a promising technology to produce green energy and realize net-zero carbon communities by shifting our reliance away from heavily polluting non-renewable fossil fuels. As opposed to traditional energy power plants, photocatalysis can be realized under mild operating conditions (ambient temperature and pressure) in the presence of visible-light-responsive semiconductors to harness the energy from the sun and convert it into chemical energy.[1] Nonetheless, it is worth pointing out that the majority of studies on photocatalysis have focused on optimizing the electron reduction half-reaction (*i.e.* HER, CO_2 reduction) with less emphasis on the utilization of sluggish holes.[2,3] Sacrificial agents (*e.g.* triethanolamine, ascorbic acid, lactic acid, and sodium sulfite) are commonly employed to consume unused holes while boosting the reduction half-reaction performance as well as the lifetime of photocatalysts.[4,5] Despite these benefits, using hole sacrificial agents adds extra costs and generates useless oxidation by-products, which adds complications to the downstream management process and presents challenges for practical implementation.[6] As such, the active engagement of photoinduced holes in the oxidation reaction is required to produce value-added products in addition to hydrogen.[7,8]

---

[a] *School of Energy and Chemical Engineering, Xiamen University Malaysia, Sepang, Selangor Darul Ehsan, 43900, Malaysia. E-mail: weejun.ong@xmu.edu.my; ongweejun@gmail.com; Web:* **https://sites.google.com/site/wjongresearch/**

[b] *Center of Excellence for NaNo Energy & Catalysis Technology (CONNECT), Xiamen University Malaysia, Sepang, Selangor Darul Ehsan, 43900, Malaysia*

[c] *Multidisciplinary Platform of Advanced Engineering, Chemical Engineering Discipline, School of Engineering, Monash University, Jalan Lagoon Selatan, Bandar Sunway, 47500 Selangor, Malaysia*

[d] *State Key Laboratory of Physical Chemistry of Solid Surfaces, College of Chemistry and Chemical Engineering, Xiamen University, Xiamen, 361005, China*

[e] *Gulei Innovation Institute, Xiamen University, Zhangzhou 363200, China*

[f] *Shenzhen Research Institute of Xiamen University, Shenzhen, 518057, China*

† Electronic supplementary information (ESI) available. See DOI: **https://doi.org/10.1039/d3ta04204a**

Notably, the transformation of aromatic alcohols to aldehydes (*e.g.* benzaldehyde and furfuraldehyde) is an essential reaction in various organic synthetic chemical industries, providing primary intermediates to hundreds of building blocks for fine chemical synthesis.[9] Recently, the selective oxidation of benzyl alcohol to its corresponding aldehyde (benzaldehyde) using photogenerated holes has emerged as a potent alternative to the conventional halogen-involving industrial process.[10–13] However, the use of additional additives (*e.g.* TEMPO)[14,15] and organic solvents (*e.g.* acetonitrile and benzotrifluoride)[16–18] makes the system more complicated and thus produces unwanted hazardous waste at the end of the reactions. In light of this, an eco-friendly catalytic system using an all-in-one noble-metal-free photocatalyst is required to utilize both photoinduced electrons and holes in the redox coupling reaction to simultaneously produce high-energy-density fuels and value-added chemical products.[19–21]

Among the myriad of semiconductors, ternary zinc indium sulfide ($ZnIn_2S_4$) with its superior visible-light responsiveness, unique electronic structure, excellent optical performance, tunable band gap, robust stability and low toxicity has emerged as a rising star in this field.[22,23] Generally, it exhibits two major crystal structures: the thermodynamically stable hexagonal phase and high-pressure cubic phase, where hexagonal $ZnIn_2S_4$ shows excellent performance in various photocatalytic processes.[24] This is due to the desirable band positions from −0.85 V to +1.56 V *vs.* NHE,[25] which are suitable for many cooperative coupling reactions such as overall water splitting where the redox potentials of H^+/H_2 and H_2O/O_2 are −0.41 V and +0.82 V *vs.* NHE, respectively.[26] On top of that, morphology plays an important role in the effective transfer of electrons and holes across the interfaces. Inspired by our previous work,[27–29] ultrathin two-dimensional (2D) nanosheets are considered to be one of the ideal morphologies for $ZnIn_2S_4$ photocatalysts. Particularly, ultrathin sheet-like layers with more exposed active sites and shorter transfer pathways are beneficial for the rapid dissociation and migration of photogenerated carriers as well as the quick diffusion of the reactant to the catalytic sites.[30] Chen *et al.*[31] and Yang *et al.*[32] successfully synthesized $ZnIn_2S_4$ nanosheets *via* a post-exfoliation method. Meanwhile, Li *et al.*[33] and Chen *et al.*[34] employed an oil-bath heating method with continuous stirring to acquire 2D $ZnIn_2S_4$. However, these approaches for acquiring $ZnIn_2S_4$ nanosheets lead to irregular shape morphologies.[35,36]

Moreover, to the best of our knowledge, few papers have reported ultrathin $ZnIn_2S_4$ nanosheets with noticeable porous structures. Henceforth, it is of vital importance to develop a one-pot solvothermal process, which can be used to precisely tune the desired morphology of $ZnIn_2S_4$. Trisodium citrate is well-known for its size-controlling and shape-directing capability in advanced materials synthesis.[37,38] Typically, it has been employed to adjust the nucleation growth of gold nanoparticles with controllable particle size, where an appropriate amount of trisodium citrate will lead to desirable monodisperse gold nanoparticles.[39] Apart from the morphology and size tuning effect, citrate ions can also induce a porous structure on the synthesized materials.[40] As exemplified by Cai *et al.*, a series of porous zinc oxide (ZnO) samples was successfully synthesized *via* the trisodium citrate-assisted synthesis route.[41] Similarly, Kim *et al.* fabricated porous carbon materials (PCMs) with interconnected hierarchical pore structures and a large pore volume of 1.19 $cm^3\ g^{-1}$ under the assistance of trisodium citrate, which showed an appreciably enhanced supercapacitor performance.[42] Moreover, Devi and Singh demonstrated the formation of a porous structure on Sm^{3+}-doped yttrium orthophosphate nanoparticles under the influence of trisodium citrate, giving rise to particular luminescent properties.[43] Motivated by these exciting reports, our interest was sparked to modulate the morphology and porosity in $ZnIn_2S_4$ materials by carefully tuning the concentration of trisodium citrate.

In this work, we successfully synthesized ultrathin $ZnIn_2S_4$ nanosheets with abundant nanopores by carefully tuning the concentration of trisodium citrate in the synthesis medium. The as-synthesized photocatalyst was employed in the dual-redox hydrogen evolution reaction coupled with benzyl alcohol (BA) oxidation for the highly selective production of benzaldehyde without the use of cocatalysts or sacrificial agents. As a result, the optimal 2D $ZnIn_2S_4$ nanosheets showed a remarkably improved photocatalytic activity, thanks to the synergistic effect of ultrathin layers and the presence of nanopores. The former endows the photocatalyst with a high specific surface area, which allows maximum light penetration and contact surface with the reactants, while the latter provides more catalytic sites for the reaction to take place. *In situ* electron paramagnetic resonance (EPR) studies elucidate that the carbon-centered (Cα) radicals are the main drivers to this fascinating reactivity, where the direct involvement of holes in C–H bond activation results in highly selective benzaldehyde production.

2. Experimental section

2.1 Synthesis of hexagonal ultrathin $ZnIn_2S_4$ nanosheet with nanopores

In the typical solvothermal synthesis, 68 mg $ZnCl_2$, 221 mg $InCl_3$ and 400 mg trisodium citrate were added into a solution containing 25 mL deionized water and 5 mL ethylene glycol. After being stirred vigorously for 30 min, 150 mg thioacetamide (TAA) was added into the solution. After another 30 min of vigorous stirring, the solution was transferred into a 100 mL Teflon-lined stainless-steel autoclave and kept at 120 °C for 12 h in an oven. After natural cooling to room temperature, the products were collected by centrifugation, rinsed with ethanol and deionized water, three times each, and dried at 60 °C overnight. The yellowish sample was finally collected and denoted LZIS-4. The amount of trisodium citrate was varied to 200, 300, 500 and 600 mg and the samples were denoted as LZIS-*x*, where *x* represents 2, 3, 4, 5 and 6, which corresponds to the amount of trisodium citrate used. Pristine flower-like $ZnIn_2S_4$ (denoted as FZIS) was acquired by following a similar procedure without adding trisodium citrate.

2.2 Preparation of the LZIS-4 thin films

Typically, 15 mg of the LZIS-4 powder was dispersed into 1 mL of ethanol and then sonicated for 30 min to obtain a colloidal solution. The thin film was prepared by drop-casting 400 μL of the colloidal solution onto fluorine-doped tin oxide (FTO) coated glass with 1.5 × 2 cm dimensions. Then the film was dried at 60 °C overnight.

2.3 Materials characterization

The details of the characterization are presented in the ESI Note 1.†

2.4 Photocatalytic dual-redox reaction

The details of the photocatalytic reaction were presented in the ESI Note 2.†

2.5 Photoelectrochemical measurements

Photoelectrochemical measurements including electrochemical impedance spectroscopy (EIS), Mott–Schottky, linear sweep voltammetry (LSV) and transient photocurrent responses tests (TPC) are presented in the ESI Note 3.†

3. Results and discussion

3.1 Synthesis, structural and morphology

Fig. 1 shows the morphology and the phase structure of $ZnIn_2S_4$ with the modification of trisodium citrate, which acts as a shape-directing agent. Pristine $ZnIn_2S_4$ synthesized *via* a solvothermal reaction shows typical nanoflowers composed of a nanosheet structure (Fig. 1a). As opposed to the regular flower-like structure, $ZnIn_2S_4$ presents a sheet-like structure with high porosity induced when an appropriate amount of trisodium citrate is added as the nucleating agent and growth agent, as depicted in Fig. 1b. It can be observed that LZIS-4 is endowed with coarse surfaces composed of a few nanosheets interweaving with each other. Specifically, LZIS-4 shows ultrathin

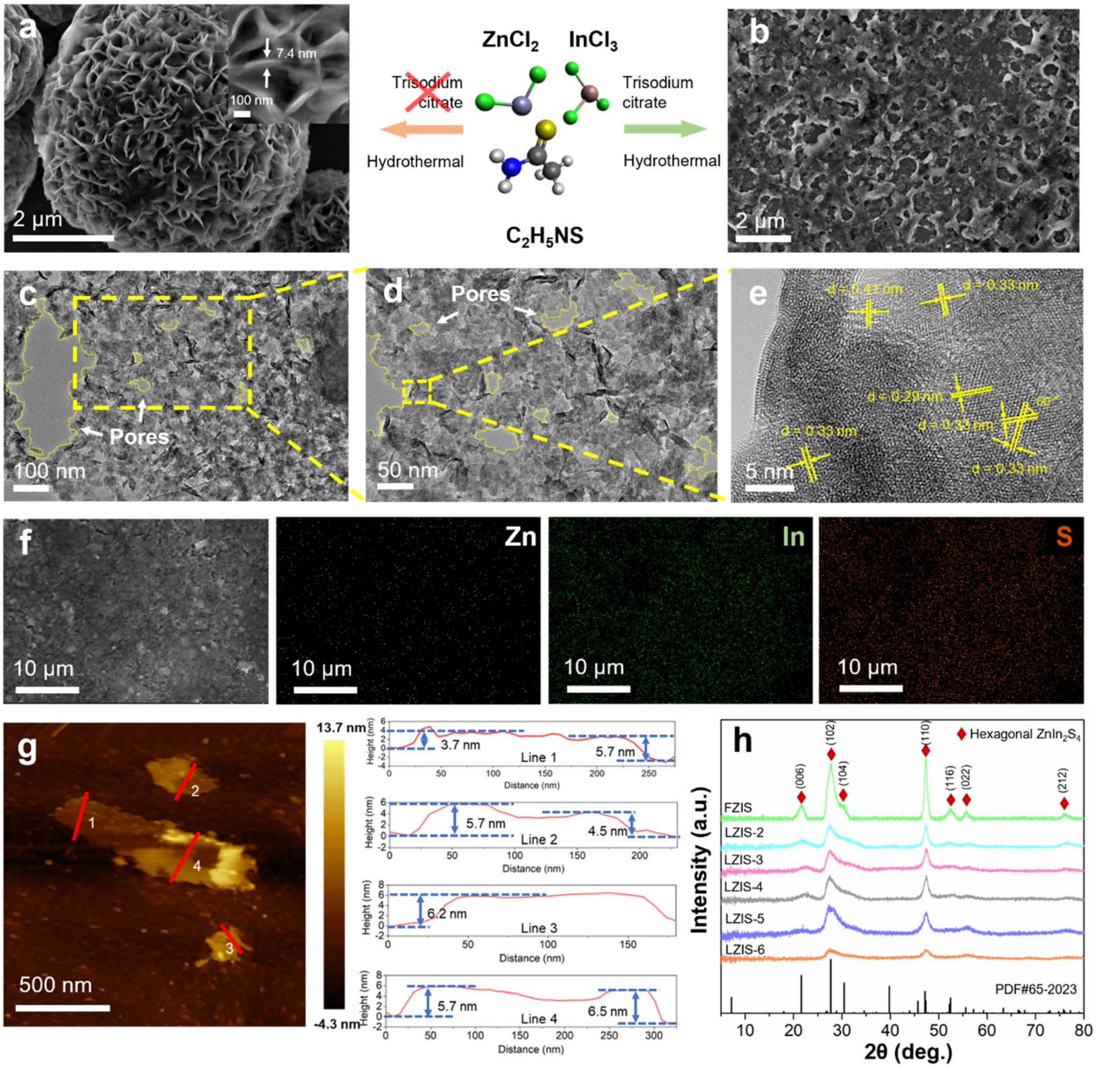

Fig. 1 FESEM images of (a) pristine $ZnIn_2S_4$ nanoflowers and (b) LZIS-4. The inset of (a) depicts the thickness of the pristine $ZnIn_2S_4$ nanoflowers. (c and d) TEM and (e) HRTEM images of LZIS-4. (f) FESEM-EDX mapping images of LZIS-4, where white, green and red represent Zn, In and S, respectively. (g) AFM topographic image and the corresponding height profiles of LZIS-4. (h) XRD of the as-prepared $ZnIn_2S_4$ samples.

nanosheets of around 4–6 nm as evidenced by atomic force microscopy (AFM) in Fig. 1g, indicating three to five S–Zn–S–In–S–In–S molecular layers.[44] This is because trisodium citrate can bind to the crystal planes or facets of the $ZnIn_2S_4$ nanoparticles, thus avoiding agglomeration during the solvothermal process while directing the growth of $ZnIn_2S_4$ along the plane direction.[45] It is further observed from the high-resolution transmission electron microscopy (HRTEM) images (Fig. 1c–e and S1†), where irregular nanopores of 10–70 nm are observed on the sheet layer of LZIS-4, revealing desirable active sites for the photocatalytic reaction. Furthermore, no discontinuous lattice spacing can be observed, denoting that the crystallinity was retained with the modification of trisodium citrate. The interplanar lattice spacing of 0.41, 0.33 and 0.29 nm can be clearly observed, which is well aligned with the (006), (102) and (104) facet plane of hexagonal $ZnIn_2S_4$, respectively. The corresponding dihedral angle of 60° also represents the typical [001] orientation of the hexagonal close-packed (HCP) structure of $ZnIn_2S_4$.[46] EDX mapping images (Fig. 1f) show evenly distributed Zn, In and S elements in the as-synthesized materials.

In short, an appropriate amount of trisodium citrate plays an important role in regulating the morphology of $ZnIn_2S_4$ from nanoflowers to nanosheets and even creating a porous structure. During the solvothermal process at elevated temperatures, citrate ions will oxidize into acetone dicarboxylic acids, which then further oxidize to produce formic acid, formaldehyde and CO. The generation of these gases leads to the formation of nanopores on the sheet-like $ZnIn_2S_4$.[37,42] However, excess trisodium citrate hinders the dispersion of $ZnIn_2S_4$ nanoparticles and causes aggregation in the $ZnIn_2S_4$ structure, which greatly reduces its surface area, as shown in Fig. S2 and Table S1.† This is because citrate ions at too high a concentration can interact strongly with each other and thus form larger clumped particles as discovered by Turkevich *et al.* and Frens who reported formation of larger gold nanoparticles when excess trisodium citrate was used.[37,47]

XRD was used to ensure the desirable crystal plane of the synthesized materials. As shown by the XRD (Fig. 1h), all the $ZnIn_2S_4$ samples exhibited similar diffraction peaks without any shift, where peaks at 21.6°, 27.7°, 30.5°, 47.2°, 52.4°, 55.6° and 75.8 correspond well to the (006), (102), (104), (110), (116), (022) and (212) planes of hexagonal $ZnIn_2S_4$ (PDF # 65-2023). This observation highlights the successful synthesis of pure $ZnIn_2S_4$ *via* a simple one-pot solvothermal method without undesirable metal oxides (*e.g.* zinc oxide or indium oxide) or other impurities. It was also proven that the addition of trisodium citrate does not damage or change the phase structure of $ZnIn_2S_4$, which retains its original crystal facets. However, FZIS has sharper peaks than the other samples, which is attributed to the larger crystalline grain of its flower-like structure (Fig. 1a) compared to the few-layered nanosheet structure of LZIS-4. It is notable that excess trisodium citrate of 600 mg greatly reduces the crystallinity of the $ZnIn_2S_4$ as evidenced by the diminished peak intensity at 21.6°, 30.5° and 52.4°.

The specific surface area and porosity of the synthesized materials are further verified by the Brunauer–Emmett–Teller (BET) and Barrett, Joyner, and Halenda (BJH) method, respectively, using the N_2 adsorption–desorption approach. As shown in Fig. S3,† FZIS, LZIS-3, LZIS-4 and LZIS-6 exhibit a consistent type IV isotherm with a hysteresis loop in the relative pressure of 0 to 1, which indicates that all the tested samples have a porous structure. The surface area of pristine FZIS is gradually increased from 60.18 $m^2 g^{-1}$ to 66.30 $m^2 g^{-1}$ (LZIS-3) and boosted up to 132.25 $m^2 g^{-1}$ in LZIS-4, thanks to the successful formation of the ultrathin nanosheet morphology, which is highly beneficial for the enhanced surface–reactant interaction. However, the surface area drastically decreases to 56.59 $m^2 g^{-1}$ when excessive trisodium citrate is used in LZIS-6, resulting from the clumped and aggregated particles. The BJH pore distribution curve (Fig. S3†) shows that the LZIS-4 has an overall higher pore volume than LZIS-3 and FZIS with the pore width ranging from 37.86 to 67.26 nm, evincing the formation of more pores within the LZIS-4 nanosheets. This observation is also in agreement with the nanopores measured in HRTEM images (Fig. 1c and d). This result further confirms that LZIS-4 exhibits an enlarged surface area with the formation of abundant nanopores on the 2D ultrathin nanosheets, which greatly promotes the photocatalytic reactivity *via* more exposed surface active sites. In contrast, the considerably high pore volume of LZIS-6 is mainly due to the irregular voids and porosity within the aggregated architecture, as shown in Fig. S2.†

3.2 Surface chemical state, functional group and optical properties

X-ray photoelectron spectroscopy (XPS) is utilized to explore the surface composition as well as the chemical state. All Zn, In and S peaks are found in the survey spectrum (Fig. 2a) of LZIS-4 and no detectable shift is observed compared to pristine $ZnIn_2S_4$, as reported in the previous literature,[48] implying the retained chemical state after modification with trisodium citrate. Typical emblematic peaks of divalent zinc (Zn^{2+}) are observed in LZIS-4 (Fig. 2b), which are represented by the binding energies at 1021.87 eV (Zn $2p_{3/2}$) and 1044.88 eV (Zn $2p_{1/2}$). From Fig. 2c and d, it can be seen that In $3d_{5/2}$ and In $3d_{3/2}$ of In^{3+} are found at 444.99 and 452.56 eV, respectively, while binding energies at 161.77 and 162.94 eV are identified as the S $2p_{3/2}$ and S $2p_{1/2}$ of LZIS-4, respectively. Notably, the sheet-like layered LZIS-4 shows a homogeneous dispersion in deionized (DI) water after 10 min ultrasonication and exists stably in solution even after being left to stand for 4 h (Fig. S4a†), while FIZS settles to the bottom after 4 h. This observation is associated with its strong negatively charged surface with a zeta potential value of −36.7 mV (Fig.-S4b†), which can be ascribed to the strong repulsive force between LZIS-4 nanosheets, which is responsible for the stability in the colloidal suspension.

Raman spectra in Fig. 3a show three typical peaks at 250, 297.4, and 340 cm^{-1}, corresponding to the longitudinal optical mode (LO1), longitudinal optical mode (LO2), and transverse optical mode (TO2) of $ZnIn_2S_4$, respectively. No changes in peak shift are observed compared with the pristine $ZnIn_2S_4$, suggesting that the crystal structure of LZIS-4 is still retained with the use of trisodium citrate during the synthesis process. The

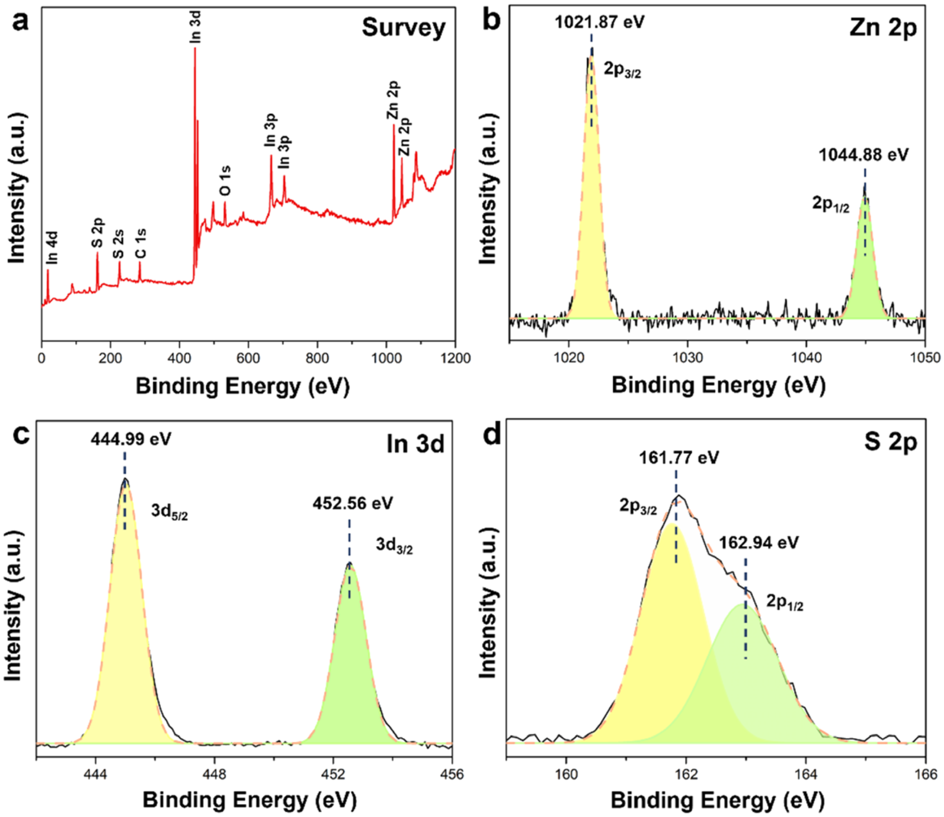

Fig. 2 (a) XPS survey spectra and high-resolution XPS spectra of (b) Zn 2p, (c) In 3d, and (d) S 2p in LZIS-4.

Fourier transform infrared spectroscopy (FT-IR) of the trisodium citrate-modified $ZnIn_2S_4$ samples show similar peaks to FZIS, indicating that the desired samples are successfully synthesized without any impurities (Fig. 3b). Three typical peaks are observed at 3339, 1618, and 1398 cm^{-1}, which are attributed to the presence of hydroxyl groups on the catalyst surface.[48] Notably, hydroxyl groups are not removed with the addition of trisodium citrate, which endow modified-$ZnIn_2S_4$ with excellent hydrophilicity and thus facilitate interaction with water molecules. On the other hand, the peak at 500 cm^{-1} is assigned to the S–S stretching vibration.[49] Meanwhile, the morphology changes and the induced nanopores could also affect the band gap of $ZnIn_2S_4$. As shown in Fig. 3c, the light-harvesting capability is examined using the UV-vis diffuse reflectance spectrum (UV-vis DRS) and all the $ZnIn_2S_4$ samples show good light responsiveness in both UV and visible-light regions. The intrinsic absorption edge of the LZIS-3 and LZIS-4 is blue-shifted compared with that of FZIS. Moreover, it can be seen that LZIS-3 and LZIS-4 experience an increasing bandgap while the rest of the modified $ZnIn_2S_4$ samples (LZIS-2, LZIS-5 and LZIS-6) have a narrower bandgap compared to the parent $ZnIn_2S_4$ (Fig. 3d). This observation is in conjunction with the reported literature,[50] where the orange-yellow samples exhibit decreasing bandgap while samples with a lighter yellow colour show the opposite trend. The blue-shifted absorption wavelength and the increasing bandgap of LZIS-3 and LZIS-4 are mainly due to the quantum confinement effect resulting from the decreasing size of the nanosheet-like $ZnIn_2S_4$. This is thanks to the appropriate amount of trisodium citrate being used, which prevents particle agglomeration during the synthesis process, as confirmed by FESEM and HRTEM analysis (Fig. 1b–d and S1†).[51] A similar blue-shifted phenomenon has also been reported when the $ZnIn_2S_4$ was exfoliated into a thin nanosheet structure.[36,52]

3.3 Photocatalytic performance

Next, all the prepared $ZnIn_2S_4$ samples were tested for their photocatalytic performance to produce hydrogen and benzaldehyde in 60 mL aqueous solution with 1 vol% benzyl alcohol (BA) under AM 1.5 light irradiation. From the time-dependent photocatalytic activity (Fig. 4a), all $ZnIn_2S_4$ samples can be seen to show increasing hydrogen production over 4 h without deactivation. Overall, LZIS-2, LZIS-3 and LZIS-4 show ameliorated hydrogen evolution performance compared to their FZIS counterpart (Fig. 4b). The optimal rate of 3.98 mmol g^{-1} h^{-1} is acquired at LZIS-4, which is an approximately 2-fold enhancement compared to that of pristine FZIS (2.08 mmol g^{-1} h^{-1}). Based on the production rate, solar-to-hydrogen (STH) efficiency under AM 1.5 light irradiation is calculated to be 0.204%. The enhancement of photocatalytic reactivity in the BA aqueous solution is due to the formation of the ultrathin nanosheet structure (Fig. 1c), which allows effective light absorption and rapid electron transfer from bulk to surface catalytic sites. It also results in a large surface area, which is highly beneficial for

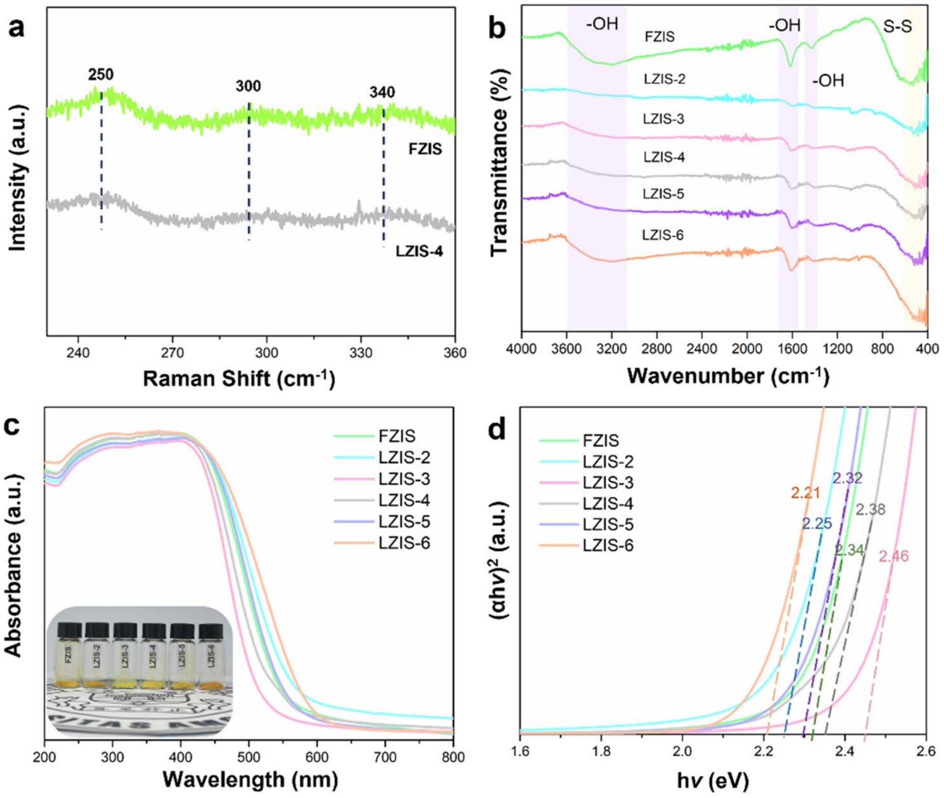

Fig. 3 (a) Raman spectra of FIZS and LZIS-4. (b) FT-IR. (c) UV-vis spectra together with the sample powder (inset) and (d) Tauc plot of the as-prepared $ZnIn_2S_4$ samples.

the interaction between reactants and the active species. The abundant nanopores which appear on the catalyst surface as evidenced by HRTEM also act as catalytic sites for the reaction to take place. When the amount of trisodium citrate used exceeds 400 mg, LZIS-5 and LZIS-6 show degraded photocatalytic activity compared to pristine FZIS. This can be explained by the role of trisodium citrate where it regulates the structure of $ZnIn_2S_4$ into thin nanosheets with enhanced activity. However, excess trisodium citrate will cause serious agglomeration and thus destroy the desirable structure, which limits the penetration of light to the active sites and restricts the surface contact between active species and the reactants (Fig. S2 and Table S1†). A similar trend is observed when the photocatalytic reactions of all the $ZnIn_2S_4$ samples are carried out under visible light ($\lambda > 420$ nm) irradiation (Fig. S5†). This has further implied that the structural-dependent photocatalytic performance plays an important role in this work despite the use of different light irradiation. Meanwhile, the supernatant liquid products from the reaction are collected and analyzed using high-performance liquid chromatography (HPLC). From Fig. 4c, similar to the observation from H_2 evolution, LZIS-4 presents the optimal benzyl alcohol conversion (23%) at 0.33 mmol h^{-1} benzaldehyde production yield with 96% selectivity. This shows the superiority of the cocatalyst-free LZIS-4 system in utilizing both electrons and holes in the redox coupling reaction to produce H_2 and value-added benzaldehyde products without using any sacrificial agents. The best sample, LZIS-4 is then tested for its chemical durability. LZIS-4 can maintain its dual-redox photocatalytic reactivity for a continuous run of 3 cycles (12 h) (Fig. 4d). As shown in Fig. S6,† the spent LZIS-4 shows a well-retained phase structure and no impurity peaks were detected, manifesting its superior stability in the organic aqueous solution. In addition to the sustained H_2 evolution, an additional 31% benzyl alcohol is further oxidized after 12 h reaction. The reaction medium is obviously changed from a yellowish solution to a dirty brown color after the photocatalytic reaction (Fig. 4h).

As shown in Fig. 4e, a series of control experiments are performed to identify the main driver of the reaction. Experiments in the dark or without photocatalysts show negligible H_2 evolution, suggesting that light and photocatalyst are the predominant factors that govern photocatalysis processes. Moreover, when water is replaced by acetonitrile, H_2 production is largely diminished (788.66 μmol g^{-1} h^{-1}), indicating both water and the dehydrogenation process of benzyl alcohol can generate protons, while the majority is contributed from water reduction. On top of that, wavelength-dependence apparent quantum efficiency (AQE) derived from the amount of generated H_2 is carried out for LZIS-4 by using various band-pass filters (Fig. 4f and Table S2†). The AQE matches with the absorption spectrum of LZIS-4 and reaches up to 5.41% at 380 nm. Considerable-high AQE and catalytic dual-redox activity of LZIS-4 is far beyond the representative photocatalysts and compatible with the majority of hybrid materials

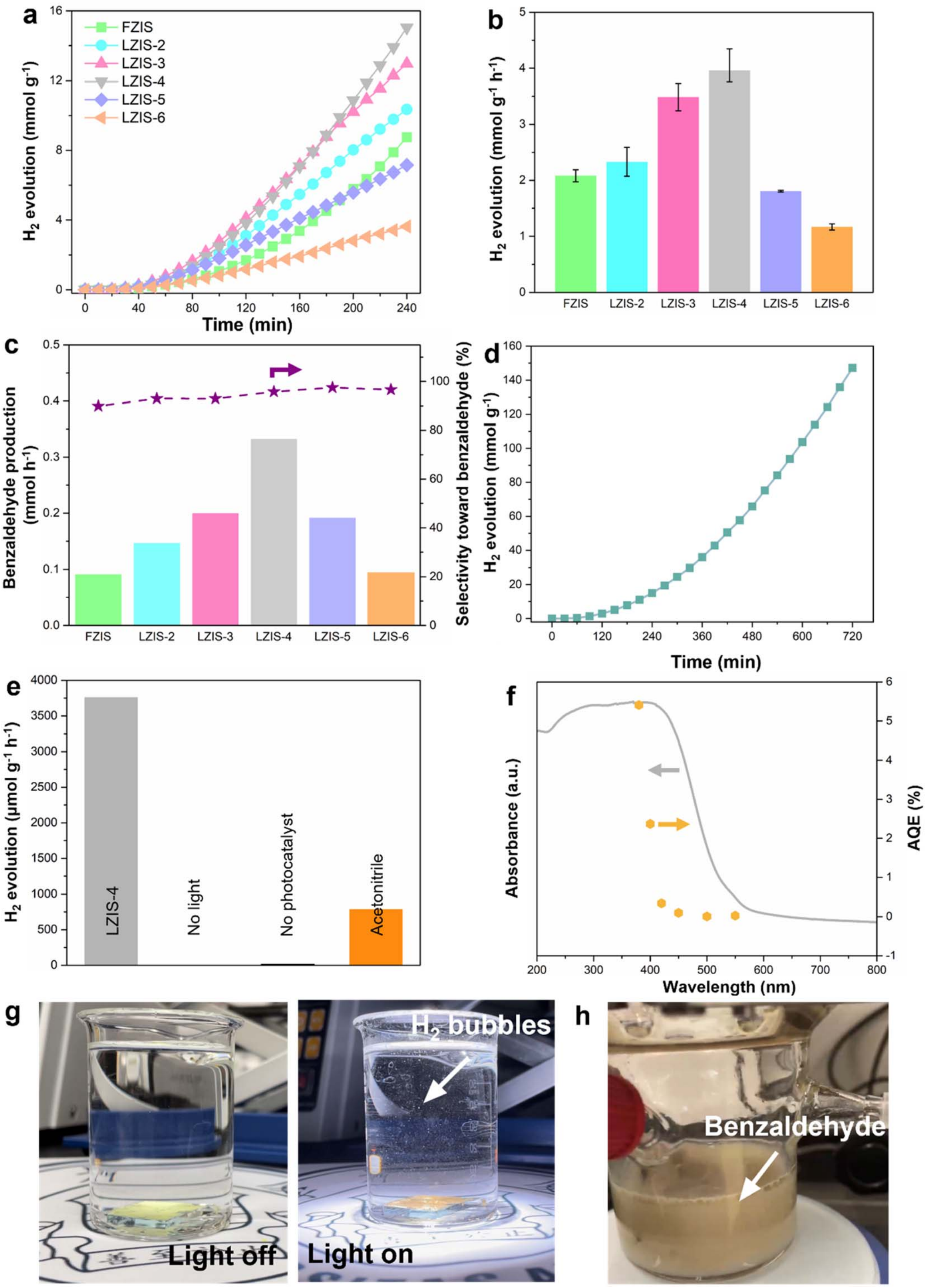

Fig. 4 (a) Time-dependent photocatalytic H_2 evolution and (b) average H_2 evolution rate over $ZnIn_2S_4$ samples under AM 1.5 light irradiation. (c) Benzyl alcohol conversion and selectivity toward benzaldehyde formation over all the $ZnIn_2S_4$ samples. (d) Prolonged stability run of 12 h for LZIS-4. (e) Control experiments using LZIS-4. (f) Apparent quantum efficiency (AQE) test of LZIS-4 at different wavelengths. (g) Digital photographs of H_2 evolution using LZIS-4 coated thin film without and with light irradiation. (h) Digital photograph of color changes of reaction medium after a 12 h dual-redox photocatalytic run with LZIS-4 as the photocatalyst.

(Table S3†). Moreover, the easy recovery of the solid substrate from the reaction medium favors the needs of large-scale industrial processes. In light of this, the optimized sample, LZIS-4 is dispersed into ethanol solution and then drop-cast onto FTO substrate (1.5 × 1.5 cm^2) to form a solid thin film. The resultant LZIS-4 thin film is employed as a photocatalyst and immersed slowly into an aqueous solution containing 1 vol% benzyl alcohol. No bubbling is observed before light irradiation as shown in Fig. 4g, while small H_2 bubbles start to appear after the light is turned on and more and more vigorous bubbling is noticed, as presented in the ESI Movie 1.† This shows the enormous potential of the fabricated photocatalyst toward practical implementation in the near future.

The photocatalytic performance of LZIS-4 in dual-redox photocatalysis was further tested using different alcohols (*e.g.* furfuryl alcohol and ethanol). As depicted in Fig. S7,† LZIS-4 achieves H_2 production rates of 1828 and 130 μmol g^{-1} h^{-1} in the presence of furfuryl alcohol and ethanol, respectively, which are 53- and 4-fold enhancements to the blank solution without the addition of alcohols. This showcases the oxidizing capability of LZIS-4 toward different alcohols while boosting the H_2 production as compared to the sluggish overall water splitting. As such, this result underlines the universality use of LZIS-4 as an all-in-one photocatalyst in multitudinous photoredox H_2 coupled with alcohol oxidation systems.

3.4 Photoelectrochemical properties

Electrochemical impedance spectroscopy (EIS), LSV and the photocurrent response are carried out to investigate the photoelectric response and electron migration impedance. Fig. 5a and b show the corresponding EIS spectra in the absence and presence of light irradiation. All the samples show decreasing arc radii when the light is turned on, indicating faster charge migration upon light activation. As can be seen from both EIS graphs, LZIS-4 displays the smallest arc diameter with the smallest R_p value of 129 kΩ (Table S4†), which reveals the lowest interfacial charge resistance across the ultrathin nanosheet layers. This gives rise to rapid charge diffusion from the surface to the active sites and hence more charge carriers can be involved in the successful reaction. In addition, from LSV (Fig. 5c), LZIS-4 shows the smallest required potential, inferring the desirably reduced overpotential of H_2 evolution, and thus favoring the generation of H_2. In addition, all $ZnIn_2S_4$ samples show consistent photocurrent intensities over 5 cycles and the photoresponse is reversible under the light on–off cycle, exemplifying good photo-stability (Fig. 5d). Among them, LZIS-4 exhibits the highest photocurrent density, denoting that the light absorption and the generation of photoinduced excitons are significantly improved while suppressing the charge recombination over its ultrathin 2D nanosheet layers with the merit of excellent light-exposure. The effective charge isolation is further confirmed by the PL spectra (Fig. S8†), where nanosheet LZIS-4 exhibits a lower PL peak intensity than the pristine flower-like FZIS. In addition, Mott–Schottky is used to determine the flat band potentials (E_{fb}) of all samples and a positive slope is observed for all $ZnIn_2S_4$ samples, demonstrating n-type semiconductors regardless the effect of trisodium citrate. As shown in Fig. S9,† E_{fb} for FZIS and LZIS-4 are −1.17 and −1.18 V *vs.* Ag/AgCl, respectively. The conduction band energy (E_{CB}) is always 0.1 V more negative than E_{fb},[53,54] which are −1.27 and −1.28 V *vs.* the Ag/AgCl, respectively, and equivalent to −1.09 and −1.10 V *vs.* NHE at pH = 7, respectively. The upshifted conduction band (CB) level bestows LZIS-4 with stronger reduction capability, which is well-evidenced from its photocatalytic performance. Based on the slope from M–S plotting, the carrier concentration is calculated for all the samples. As presented in Table S5,† the charge density increases significantly from 7.66×10^{21} cm^{-3} of FZIS to 1.17×10^{22} cm^{-3} of LZIS-4 and drastically decreases to 1.06×10^{22} cm^{-3} in LZIS-6, further confirming the enhanced amount of photoinduced carriers in the optimized trisodium citrate-modified LZIS-4. Compiling the findings, the band structures of each $ZnIn_2S_4$ sample are postulated as shown in Fig. 5e. Compared with pristine FZIS, LZIS-4 with a slightly upshifted conduction band and a more positive valence band demonstrated a better redox capability toward simultaneous H_2 and benzaldehyde production. Besides, an appropriately extended bandgap leads to an expanded absorption edge in LZIS-4, which permits generation of more photoinduced carriers.

3.5 Mechanistic insight into charge transfer and utilization

To discern the reaction mechanism, different scavengers are added to capture the active species and radicals in this system. This includes triethanolamine (TEOA), $K_2S_2O_8$ and isopropanol (IPA), which are adopted to quench photoinduced holes, electrons and hydroxyl ($^{\bullet}OH$) radicals, respectively. Fig. 6a shows that isopropanol has the least effect on the H_2 evolution as confirmed by the higher band position of the synthesized LZIS-4, which is unfavorable to meet the requirements of water oxidation to produce $^{\bullet}OH$ radicals. On the other side, H_2 evolution is drastically depressed with the involvement of $K_2S_2O_8$, inferring that the photogenerated electrons are the core active species to reduce H^+ to H_2. Interestingly, when TEOA is introduced to the system as a hole scavenger, it shows a diminished H_2 evolution rate after 4 h time. Theoretically, the quick consumption of photogenerated holes will greatly inhibit the charge recombination, hence favoring the corresponding photoexcited electrons in the reduction reaction. This is also proved by most of the photocatalytic H_2 evolution systems with the use of hole scavengers to compensate for the sluggish four electrons' oxygen evolution.[55–58] Henceforth, in this regard, the lower H_2 evolution can be attributed to the retarded dehydrogenation process of BA due to the rapid consumption of the holes by TEOA. This phenomenon also indicates that the system undergoes direct hole oxidation of BA to form benzaldehyde rather than the non-selective active free radical's route. This has been further proven by the HPLC results (Fig. 6b) where the relative conversion of benzyl alcohol appears lowest when TEOA is used to rapidly consume the holes. On the other hand, the conversion of benzyl alcohol remains at its optimum rate when $K_2S_2O_8$ or IPA is added, evincing that neither the electrons or hydroxyl radicals are responsible for direct or indirect benzyl alcohol oxidation.

In addition, electron paramagnetic resonance (EPR) with the aid of spin markers is used to further validate the aforementioned results by capturing the active species generated during the photocatalytic reaction. From Fig. 6c, when DMPO is employed to capture the $^{\bullet}OH$ radicals in the aqueous solution,

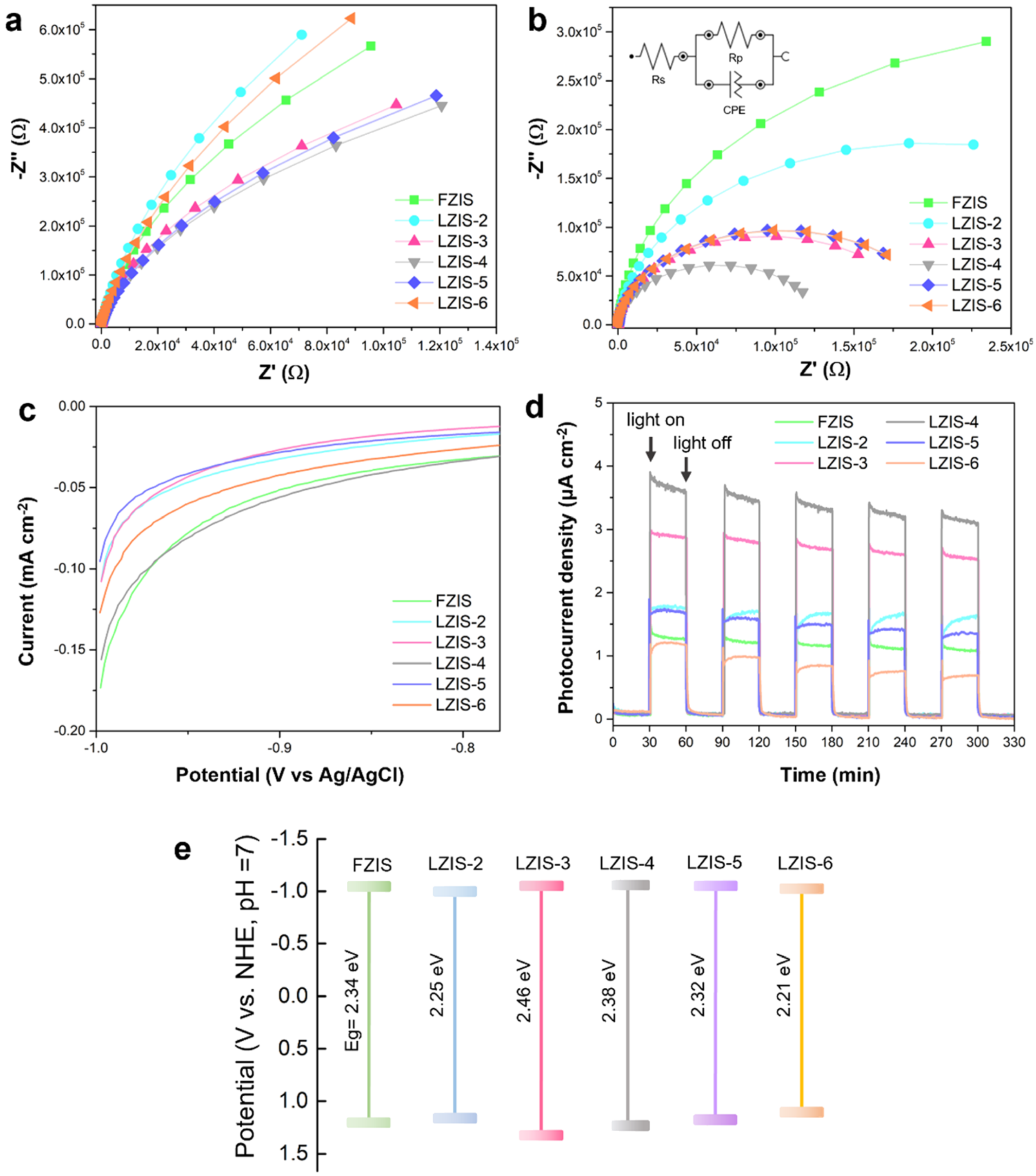

Fig. 5 EIS of all the $ZnIn_2S_4$ samples (a) without light and (b) with light. The equivalent Randles circuits are used to fit the Nyquist plots data, where R_s, R_p and CPE are the total series resistance, charge transfer resistance and double-layer capacitance, respectively (inset of (b)). (c) LSV spectra of all the $ZnIn_2S_4$ samples. (d) Photocurrent response of $ZnIn_2S_4$ samples with 30 s light on/off intervals. (e) Postulated electronic band position of $ZnIn_2S_4$ samples.

no obvious signal is observed after 10 min light irradiation, further proving that ˙OH radicals are not the main active species involved in this system. Interestingly, when DMPO is used as a carbon-centered (α-hydroxybenzyl, Cα) radical scavenger in benzyl alcohol, six typical characteristic signals with $\alpha_N = 15.1$ and $\alpha_H = 21.9$ (Fig. 6d) are observed under light irradiation, which correspond to the nitrogen and hydrogen hyperfine splitting for nitroxide nitrogen.[59,60] In this sense, LZIS-4 produces prominent peak intensity of DMPO–Cα radicals compared to that of ˙OH radicals, suggesting that the α-C–H bond activation and dehydrogenation are greatly accelerated by the surface holes of LZIS-4. The dehydrogenation process has also been verified by minor H_2 generation when water is replaced by acetonitrile, as depicted in Fig. 4c, implying a small portion of the hydrogen is derived from the dehydrogenation of benzyl alcohol.

Concluding the above experimental and characterization results, the mechanism of the enhanced photocatalytic performance of LZIS-4 under the synergistic effect of a large specific surface area and porous structure is revealed in Fig. 7. First, the excellent surface electronegativity of LZIS-4 as proved by zeta measurements (Fig. S4b†) helps to boost the adsorption of H^+ reactants as well as stimulate strong affinity to the alcohol hydroxyl group.[61,62] Upon light irradiation, ultrathin LZIS-4 nanosheets with a large surface area are greatly exposed to the photon irradiation, thus producing masses of photogenerated

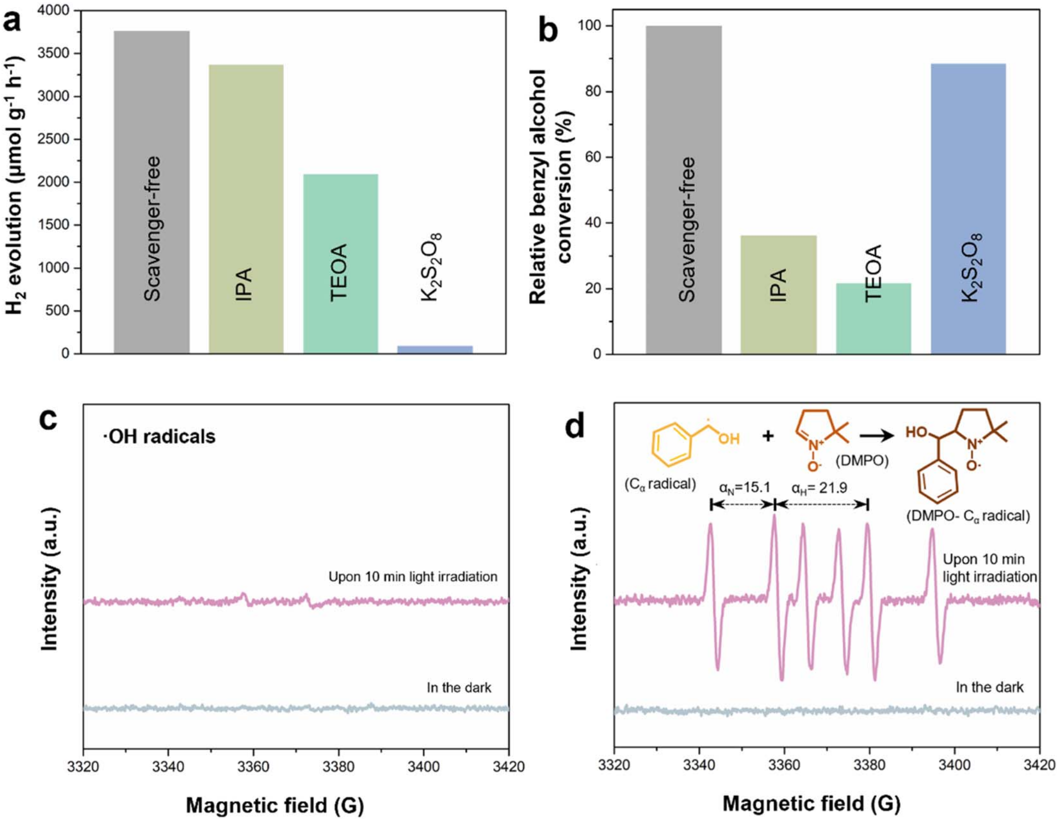

Fig. 6 Scavenger tests for the (a) H_2 evolution rate and (b) benzyl alcohol conversion. Conversion rates are normalized to 100% based on the scavenger-free sample. Condition: scavenger was added same as the mole of benzyl alcohol added. EPR spectra of (c) hydroxyl ($^{\bullet}$OH) radicals and (d) carbon-centered ($^{\bullet}$CH(OH)Ph) radicals under light irradiation over LZIS-4. The spectra are recorded at 10 min light illumination.

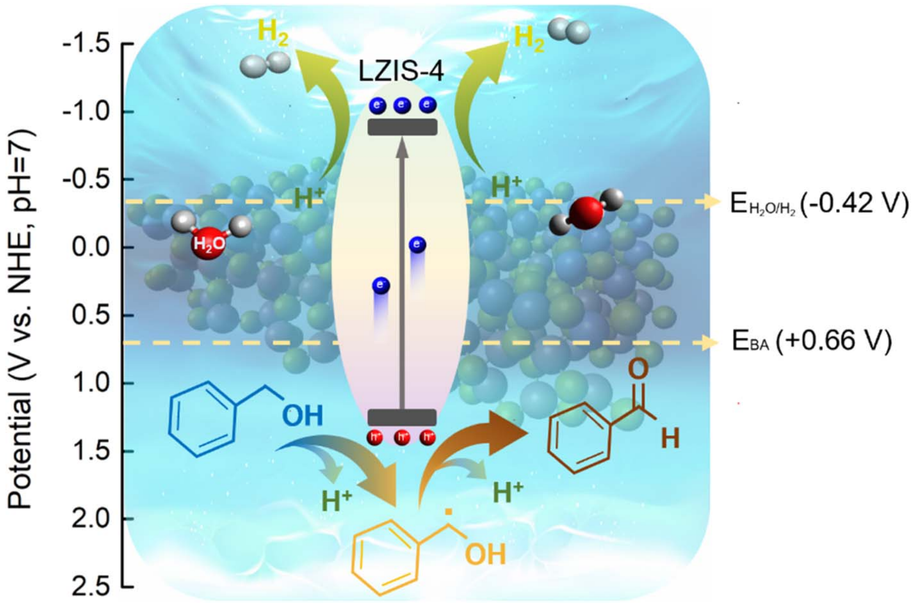

Fig. 7 A schematic of LZIS-4 in the dual coupling reaction of H_2 evolution and benzyl alcohol oxidation.

carriers. Photoexcited electrons migrate rapidly across the ultrathin layers and reach the active nanopores sites to partake in the H^+ reduction process for H_2 production while holes at the valence band oxidize benzyl alcohol into Cα radicals, which further react to form benzaldehyde. Notably, this highlights the merits of the direct involvement of holes in the C–H bond cleavage instead of the non-selective $^{\bullet}OH$ radical-induced mechanism pathway, which generates a wide variety of oxidation products.[19,63]

4. Conclusions

In summary, ultrathin $ZnIn_2S_4$ nanosheets with abundant nanopores are successfully fabricated for the effective utilization of both photogenerated electrons and holes in the dual-redox reaction. The optimal LZIS-4 shows a remarkably enhanced H_2 evolution rate of 3.98 mmol h^{-1} g^{-1} and a highly selective (96%) benzaldehyde yield of 1.32 mmol after 4 h reaction. The ameliorated photocatalytic activity is predominantly due to the formation of ultrathin nanosheet layers with abundant nanopores on LZIS-4, which is confirmed by the AFM, TEM/HRTEM, FESEM and BET characterizations. This bestowed LZIS-4 with a large specific surface area for enhanced light exposure and better interaction between the active species and the reactants. In addition, the porous structure acts as additional catalytic sites to further boost the reaction rate. In retrospect, all-in-one LZIS-4 with an appropriate band edge position, lower charge resistance and strong redox capability are capable of accelerating the dual-redox H_2 evolution coupled with benzaldehyde production. The as-synthesized LZIS-4 demonstrates a dual-redox performance surpassing that of most of the single materials. As such, this work provides a novel strategy to modulate the desirable morphology of $ZnIn_2S_4$ in overcoming the sluggish hole transfer and its utilization in dual-redox photocatalytic activity.

Conflicts of interest

The authors declare no competing financial interest.

Acknowledgements

The authors would like to acknowledge the financial support provided by the Ministry of Higher Education (MOHE) Malaysia under the Fundamental Research Grant Scheme (FRGS) (ref. no.: FRGS/1/2020/TK0/XMU/02/1). The author would also like to thank the Ministry of Science, Technology and Innovation (MOSTI) Malaysia under the Strategic Research Fund (SRF) (S.22015). The authors would also like to acknowledge the financial support provided by the National Natural Science Foundation of China (ref. no.: 22202168) and the Guangdong Basic and Applied Basic Research Foundation (ref. no.: 2021A1515111019). We would also like to acknowledge the financial support from the State Key Laboratory of Physical Chemistry of Solid Surfaces, Xiamen University (ref. no.: 2023X11). This work is also funded by Xiamen University Malaysia Investigatorship Grant (grant no.: IENG/0038), Xiamen University Malaysia Research Fund (ICOE/0001, XMUMRF/2021-C8/IENG/0041 and XMUMRF/2019-C3/IENG/0013) and Hengyuan International Sdn. Bhd. (grant no.: EENG/0003).

Notes and references

1 N. Luo, T. Montini, J. Zhang, P. Fornasiero, E. Fonda, T. Hou, W. Nie, J. Lu, J. Liu, M. Heggen, L. Lin, C. Ma, M. Wang, F. Fan, S. Jin and F. Wang, *Nat. Energy*, 2019, **4**, 575–584.
2 N. Luo, T. Hou, S. Liu, B. Zeng, J. Lu, J. Zhang, H. Li and F. Wang, *ACS Catal.*, 2020, **10**, 762–769.
3 G. Z. S. Ling, V. B.-Y. Oh, C. Y. Haw, L.-L. Tan and W.-J. Ong, *Energy Mater. Adv.*, 2023, **4**, 0038.
4 H.-T. Fan, Z. Wu, K.-C. Liu and W.-S. Liu, *Chem. Eng. J.*, 2022, **433**, 134474.
5 W. L. Jia, W. J. Li, H. Y. Yuan, X. Wu, Y. Liu, S. Dai, Q. Cheng, P. F. Liu and H. G. Yang, *J. Energy Chem.*, 2022, **74**, 341–348.
6 H. Wang, X. Gao, Z. Lv, T. Abdelilah and A. Lei, *Chem. Rev.*, 2019, **119**, 6769–6787.
7 M. Z. Rahman, T. Edvinsson and J. Gascon, *Nat. Rev. Chem*, 2022, **6**, 243–258.
8 H. Wang, H. Qi, X. Sun, S. Jia, X. Li, T. J. Miao, L. Xiong, S. Wang, X. Zhang, X. Liu, A. Wang, T. Zhang, W. Huang and J. Tang, *Nat. Mater.*, 2023, **22**, 619–626.
9 J. Li, M. Li, H. Sun, Z. Ao, S. Wang and S. Liu, *ACS Catal.*, 2020, **10**, 3516–3525.
10 L. Marzo, S. K. Pagire, O. Reiser and B. König, *Angew. Chem., Int. Ed.*, 2018, **57**, 10034–10072.
11 B. Chen, L.-Z. Wu and C.-H. Tung, *Acc. Chem. Res.*, 2018, **51**, 2512–2523.
12 J.-Y. Li, Y.-H. Li, M.-Y. Qi, Q. Lin, Z.-R. Tang and Y.-J. Xu, *ACS Catal.*, 2020, **10**, 6262–6280.
13 M. Yu, N. Wang, K. Lin, D. Song, J. Chen, T. Liang, J. Sun, K. Pan and H. Fu, *J. Mater. Chem. A*, 2023, **11**, 4302–4309.
14 H. A. Beejapur, Q. Zhang, K. Hu, L. Zhu, J. Wang and Z. Ye, *ACS Catal.*, 2019, **9**, 2777–2830.
15 J. M. Hoover and S. S. Stahl, *J. Am. Chem. Soc.*, 2011, **133**, 16901–16910.
16 J. Kou, C. Lu, J. Wang, Y. Chen, Z. Xu and R. S. Varma, *Chem. Rev.*, 2017, **117**, 1445–1514.
17 M. Zhang, Q. Wang, C. Chen, L. Zang, W. Ma and J. Zhao, *Angew. Chem., Int. Ed.*, 2009, **48**, 6081–6084.
18 Y. Chen, L. He, H.-R. Tan, X. Lin, S. Jaenicke and G.-K. Chuah, *J. Mater. Chem. A*, 2023, **11**, 12342–12353.
19 M.-Y. Qi, M. Conte, M. Anpo, Z.-R. Tang and Y.-J. Xu, *Chem. Rev.*, 2021, **121**, 13051–13085.
20 X. Xiang, B. Zhu, J. Zhang, C. Jiang, T. Chen, H. Yu, J. Yu and L. Wang, *Appl. Catal., B*, 2023, **324**, 122301.
21 X. Li, S. Lu, J. Yi, L. Shen, Z. Chen, H. Xue, Q. Qian and M.-Q. Yang, *ACS Appl. Mater. Interfaces*, 2022, **14**, 25297–25307.
22 V. B.-Y. Oh, S.-F. Ng and W.-J. Ong, *EcoMat*, 2022, **4**, e12204.
23 Y. Ren, J. J. Foo, D. Zeng and W.-J. Ong, *Small Struct.*, 2022, **3**, 2200017.
24 M. Li, L. Wang, X. Zhang, W. Yin, Y. Zhang, J. Li, Z. Yin, Y. Cai, S. Liu and Q. Zhao, *Chin. Chem. Lett.*, 2022, **34**, 107775.
25 R. Yang, L. Mei, Y. Fan, Q. Zhang, R. Zhu, R. Amal, Z. Yin and Z. Zeng, *Small Methods*, 2021, **5**, 2100887.

26 J. Di, C. Yan, A. D. Handoko, Z. W. Seh, H. Li and Z. Liu, *Mater. Today*, 2018, **21**, 749–770.
27 W.-J. Ong, L.-L. Tan, S.-P. Chai, S.-T. Yong and A. R. Mohamed, *Nano Energy*, 2015, **13**, 757–770.
28 D. Zeng, W. Xu, W.-J. Ong, J. Xu, H. Ren, Y. Chen, H. Zheng and D.-L. Peng, *Appl. Catal., B*, 2018, **221**, 47–55.
29 L.-L. Tan, W.-J. Ong, S.-P. Chai, B. T. Goh and A. R. Mohamed, *Appl. Catal., B*, 2015, **179**, 160–170.
30 G. Z. S. Ling, S.-F. Ng and W.-J. Ong, *Adv. Funct. Mater.*, 2022, **32**, 2111875.
31 J. Chen, F. Xin, X. Yin, T. Xiang and Y. Wang, *RSC Adv.*, 2015, **5**, 3833–3839.
32 H. Yang, R. Cao, P. Sun, J. Yin, S. Zhang and X. Xu, *Appl. Catal., B*, 2019, **256**, 117862.
33 L. Li, D. Ma, Q. Xu and S. Huang, *Chem. Eng. J.*, 2022, **437**, 135153.
34 K. Chen, X. Wang, Q. Li, Y.-N. Feng, F.-F. Chen and Y. Yu, *Chem. Eng. J.*, 2021, **418**, 129476.
35 D. Yang, J. Liang, L. Luo, R. Deng, G. Li, Q. He and Y. Chen, *Chin. Chem. Lett.*, 2021, **32**, 2534–2538.
36 T. Su, C. Men, L. Chen, B. Chu, X. Luo, H. Ji, J. Chen and Z. Qin, *Adv. Sci.*, 2022, **9**, 2103715.
37 J. Turkevich, P. C. Stevenson and J. Hillier, *Discuss. Faraday Soc.*, 1951, **11**, 55–75.
38 M. Sevilla, N. Díez and A. B. Fuertes, *ChemSusChem*, 2021, **14**, 94–117.
39 H. Yagyu, Y. Tanabe, S. Takano and M. Hamamoto, *Micro Nano Lett.*, 2017, **12**, 536–539.
40 D. Liu, G. Xu, X. Yuan, Y. Ding and B. Fan, *Fuel*, 2023, **332**, 126044.
41 H. Cai, Z. Guo, Q. Qiao, S. Ren, D. Zhu, P. Yin and Z. Xue, *Micro Nano Lett.*, 2019, **14**, 1244–1248.
42 E. K. Kim, B. M. Lee, J. J. Park, J. H. Choi and J. M. Yun, *Mater. Today Sustain.*, 2022, **20**, 100238.
43 H. F. Devi and T. D. Singh, *Opt. Commun.*, 2019, **439**, 34–37.
44 S. Zhang, X. Liu, C. Liu, S. Luo, L. Wang, T. Cai, Y. Zeng, J. Yuan, W. Dong, Y. Pei and Y. Liu, *ACS Nano*, 2018, **12**, 751–758.
45 M. Sheng, C. Gan, Y. Li, Z. Hu, Y. Zhang, X. Gao, X. Wang and H. Jiang, *Chem. Eng. J.*, 2022, **446**, 136919.
46 R. Pan, M. Hu, J. Liu, D. Li, X. Wan, H. Wang, Y. Li, X. Zhang, X. Wang, J. Jiang and J. Zhang, *Nano Lett.*, 2021, **21**, 6228–6236.
47 G. Frens, *Nat. Phys. Sci.*, 1973, **241**, 20–22.
48 X. Dang, M. Xie, F. Dai, J. Guo, J. Liu and X. Lu, *Adv. Mater. Interfaces*, 2021, **8**, 2100151.
49 E. J. Diana and T. V. Mathew, *Colloids Surf., B*, 2022, **220**, 112949.
50 Y. Shao, X. Hao, S. Lu and Z. Jin, *Chem. Eng. J.*, 2023, **454**, 140123.
51 B. Pan, Y. Wu, B. Rhimi, J. Qin, Y. Huang, M. Yuan and C. Wang, *J. Energy Chem.*, 2021, **57**, 1–9.
52 X. Shi, L. Mao, P. Yang, H. Zheng, M. Fujitsuka, J. Zhang and T. Majima, *Appl. Catal., B*, 2020, **265**, 118616.
53 C. Zeng, Y. Hu and H. Huang, *ACS Sustain. Chem. Eng.*, 2017, **5**, 3897–3905.
54 C. Ling, X. Ye, J. Zhang, J. Zhang, S. Zhang, S. Meng, X. Fu and S. Chen, *Sci. Rep.*, 2017, **7**, 27.
55 D. Gao, H. Long, X. Wang, J. Yu and H. Yu, *Adv. Funct. Mater.*, 2023, **33**, 2209994.
56 H. S. Moon, K.-C. Hsiao, M.-C. Wu, Y. Yun, Y.-J. Hsu and K. Yong, *Adv. Mater.*, 2023, **35**, 2200172.
57 J. Tao, M. Wang, X. Zhang, L. Lu, H. Tang, Q. Liu, S. Lei, G. Qiao and G. Liu, *Appl. Catal., B*, 2023, **320**, 122004.
58 X. Shi, L. Mao, C. Dai, P. Yang, J. Zhang, F. Dong, L. Zheng, M. Fujitsuka and H. Zheng, *J. Mater. Chem. A*, 2020, **8**, 13376–13384.
59 J. Wang, M.-Y. Qi, X. Wang and W. Su, *Appl. Catal., B*, 2022, **302**, 120812.
60 J. Wan, L. Liu, Y. Wu, J. Song, J. Liu, R. Song, J. Low, X. Chen, J. Wang, F. Fu and Y. Xiong, *Adv. Funct. Mater.*, 2022, **32**, 2203252.
61 F. Xing, R. Zeng, C. Cheng, Q. Liu and C. Huang, *Appl. Catal., B*, 2022, **306**, 121087.
62 X. Yan and Z. Jin, *Chem. Eng. J.*, 2021, **420**, 127682.
63 C. Zheng, G. He, X. Xiao, M. Lu, H. Zhong, X. Zuo and J. Nan, *Appl. Catal., B*, 2017, **205**, 201–210.